# FRACTURE MECHANICS MODEL OF NEEDLE CUTTING TISSUE

**Andrew C. Barnett**
Department of Mechanical and Nuclear Engineering
The Pennsylvania State University, University Park, PA
acb279@psu.edu

**Yuan-Shin Lee**
Department of Industrial and Systems Engineering
North Carolina State University, Raleigh, NC, USA
yslee@ncsu.edu

**Jason Z. Moore**[1]
Department of Mechanical and Nuclear Engineering
The Pennsylvania State University, University Park, PA
jzm14@psu.edu



**ABSTRACT**

*This work develops a needle insertion force model based on fracture mechanics which incorporates the fracture toughness, shear modulus, and friction force of the needle and tissue. Ex vivo tissue experiments were performed to determine these mechanical tissue properties. A double insertion of the needle into the tissue was utilized to determine the fracture toughness. The shear modulus was found by applying an Ogden Fit to the stress-strain curve of the tissue achieved through tension experiments. The frictional force was measured by inserting the needle through precut tissue. Results show the force model predicts within 0.2 N of experimental needle insertion force and the fracture toughness is primarily affected by the needle diameter and needle edge geometry. On average, the*

[1] Corresponding Author

*tearing force was found to account for 61% of the total insertion force, the spreading force to account for 18%, and the friction force to account for the remaining 21%.*

*Keywords: Needle Insertion, Tissue Cutting, Cutting Edge Geometry, Tribology*

## 1. INTRODUCTION

Needles are a commonly used instrument in medicine. They are used to deliver drugs, biopsy tissue, draw blood, conduct brachytherapy radiation cancer treatment, and in many other medical procedures [1]. Low insertion force is critical in these procedures for two reasons: first, a low insertion force has been shown to reduce the pain felt in patients [2]; second, lower insertion force allows for more accurate needle tip placement by reducing tissue deflection and needle bending [3].

Brachytherapy is an example of a procedure that requires precise needle accuracy for the placement of radioactive seeds to kill cancer cells. The needle insertion force between the tissue and needle hinder placement accuracy. The insertion force causes the needle to bend, as seen in Figure 1(a). The insertion force also causes the target movement, as shown in Figure 1(b). Unlike in traditional manufacturing processes where the work piece is rigidly clamped, the tissue is free to move so the target can easily become displaced upon needle insertion. Lower insertion force has shown to reduce needle bending and tissue deflection [3].

Work has been done to reduce the insertion force of needles by altering tip geometries and reducing the gauge size. Needle geometries have been modelled in order to define a more efficient cutting geometry [4-6]. This leads to different tip

geometries (bevel, lancet point, triangular, etc.) being created to reduce the insertion force [7-9]. Smaller needles, including microneedles (needles that are sometimes only 100 μm in diameter) are now being used in procedures to drastically reduce the insertion force [10]. However, microneedles cannot be used in all procedures. For example, vaccinations that require a large dose or have large particulates require a needle of sufficiently large diameter [11].

The dynamic effects of insertion on cutting force have been briefly explored in tissue cutting literature. Work has been carried out exploring the effect of needle rotation on insertion mechanics [12, 13]. Applied vibration has also been explored by researchers for cutting tissue [14-18]. Another dynamic method of insertion is to increase the needle insertion speed. Heverly et al. has shown that with increasing the insertion speed of the needle, the force needed to puncture the tissue is reduced in porcine heart [19]. Higher insertion speed has also been shown to reduce tissue deflection in porcine hearts [20], porcine liver samples [21], and turkey breast [22]. However, for tougher tissues such as skin, the reduction in insertion force is not seen with higher velocities. Frick et al. showed no velocity dependence of insertion force on the insertion of suture needles into sheep skin [23]. In a skin like simulant, Koelmans et al. found that the insertion force increases 12% by increasing the insertion speed from 100 μm/s to 500 μm/s [24]. A force model is needed to describe the velocity dependent phenomena occurring in the needle-tissue interactions.

Accurate models of needle force interaction can allow for the development of more accurate needle insertion instruments. Several physics and nonphysics based

models have been developed to predict insertion forces. Many models have been created to fit the insertion force profile without using any physical parameters in the model [19, 25, 26]. Further, other models looked at incorporating mechanics of cutting into the models by looking at the forces acting on the needle [8, 27, 28]. These models broaden the utilization across different medium and needle geometries; however they do not develop fundamental knowledge on how these forces are created. Shergold and Fleck developed a fracture mechanics based model to describe the forces acting on the needle for quasistatic insertion, and is the basis of the model presented in this work [29]. Mirsa et al. utilized fracture mechanics concepts to determine the mechanics of steerable needles in tissues [30]. However, dynamic insertion models have only briefly been utilized. Mavash et al. developed a force model for dynamic insertion of needles by using the Modified Kelvin model to describe the tissue [31]. The work presented in this paper develops a fracture mechanics based model to describe dynamic needle insertion.

Fracture mechanics based approaches have been used extensively on metallic and ceramic materials because of its ability to better predict when failure will occur [32, 33]. In addition, fracture mechanics based models have been applied to cutting of traditional manufacturing materials [34-36]. Recently, researchers have been applying fracture mechanics techniques to highly deformable materials including biological materials [37-39]. By measuring the energy to fracture tissue and moving a needle through the newly developed crack, an accurate physics-based force model is constructed in this paper. The fracture mechanics model incorporates parameters

including fracture toughness and shear modulus of the tissue. Because of the viscoelastic properties of the tissue, these factors are strain rate dependent, causing the speed of insertion to vary the insertion force. In addition, the model developed incorporates a frictional component. Researchers have found that the friction force between the needle and the tissue is dependent on insertion speed [8, 40].

This study investigates the fracture mechanics of porcine skin and develops a physics based model to explain the dynamic needle-tissue interaction. This model explores the physical parameters of the tissue to determine how the velocity of insertion affects their properties. Porcine skin was chosen as the testing medium for this work, as researchers in the past have used it as an appropriate analog to human skin [41]. Hypodermic needles of various sizes were used in this study, as they are commonly used in the medical field. This paper describes the mechanics of tissue cutting as well as the fracture mechanics model developed to describe the cutting. Experiments were conducted to determine the mechanical properties of the tissue as well as the needle-tissue interaction. For each parameter, a model was fit to the resultant data. Once all the parameters were determined, they were incorporated into the final model and validated with experimental data.

## 2. NEEDLE INSERTION MECHANICS

### 2.1 Needle Insertion Forces

As the needle inserts through a 4 mm section of porcine tissue with no backing, there are three phases, as shown in Figure 2. In Phase 1, the tissue deflects and the force gradually rises. In Phase 2 the tissue is cut; an initial crack is formed, the crack is widened by the needle geometry, and the needle passes through with friction acting between the needle and the tissue. In Phase 3 the needle continues to pass through the tissue and there is friction force between the outside of the needle and the tissue. If the needle was passing through a thicker tissue there may be multiple deflection and cutting phases before the needle reaches its target location. The maximum cutting force is reached in Phase 2 and is defined as the total cutting force, $P$ as shown in Figure 2. The three forces that make up $P$ are the tearing force ($P_t$) that tears the tissue forming a crack, the force ($P_s$) needed to spread the tissue apart to allow the needle through, and the friction ($P_F$) that acts between the needle and the tissue as shown in Figure 3 and Equation 1. The fracture mechanics model focuses on determining $P$.

$$P = P_t + P_s + P_F \tag{1}$$

### 2.2 Fracture Mechanics Model

A tissue fracture mechanics model is formed dependent on needle diameter and insertion speed. As the needle inserts into tissue, work is performed equal to $P\delta l$ where $P$ is the force exerted and $\delta l$ is a differential insertion length. The needle then creates a crack in the tissue and spreads the tissue apart to accommodate the width of

the needle. During cutting, there is friction between the needle and tissue as well. The work done by the needle is equal to the energy released by the creation of the crack $\delta W_R$, the strain energy stored by the tissue spreading around the needle $\delta\Lambda$, and the work done by the friction on the needle $P_F(l) \cdot \delta l$, where the friction is a function of insertion depth $l$. This relationship produces Equation 2:

$$P\delta l = \delta W_R + \delta\Lambda + P_F(l) \cdot \delta l \tag{2}$$

The work released by the generation of a crack in the tissue, $\delta W_R$, is:

$$\delta W_R(d,v) = J_{IC}(d,v)\, a(d)\, \delta l \tag{3}$$

Where $a(d)$ is the length of the crack generated in m, $J_{IC}(d,v)$is the mode-I fracture toughness of the tissue in J/m$^2$, $d$ is the outer diameter of the needle in m, and $v$ is the insertion speed of the needle in m/s. Kinetic energy was neglected in the development of the model due to its contribution in the work-energy equation being in the range of micro-Joules when a relatively small mass of tissue is acted upon. In experiments performed in Section 3.1, only 3.3*10$^{-4}$ kg of tissue is acted upon.

The strain energy $\delta\Lambda$ associated with the spreading of the tissue can be modelled as spreading a circle with an initial radius $r = 0$ to final radius $r = R$. With a plane strain assumption, this reduces to:

$$\delta\Lambda = \tfrac{1}{2}\, \pi\, \mu(v)\, R^2\, \delta l \tag{4}$$

However, the crack around the needle is not completely circular [37]. Because of this, a nondimensional contact factor $f(d)$ needs to be added into the $\delta\Lambda$ term. Absorbing the constants, Equation 4 then becomes:

$$\delta\Lambda = \mu(v)\, R^2 f(d)\, \delta l \tag{5}$$

Substituting Equations 3 and 5 into Equation 2 yields:

$$P(d,v)\,\delta l = J_{IC}(d,v)\,a(d)\,\delta l + \mu(v)\,R^2 f(d)\,\delta l + P_F(l,d,v)\cdot\delta l \quad (6)$$

The goal of this work is to be able to describe the maximum insertion force of the needle into tissue. The friction occurring at the maximum insertion force is the puncture friction force $P_{FP}$. This friction force is substituted into Equation 6. Assuming the tissue parameters do not change with depth and describing only the maximum insertion force, Equation 6 becomes:

$$P(d,v) = J_{IC}(d,v)\,a(d) + \mu(v)\,R^2 f(d) + P_{FP}(d,v) \quad (7)$$

In order to determine the mechanical properties of fracture toughness $J_{IC}$ and shear modulus $\mu$, as well as the needle-tissue interaction components crack length $a$ and puncture friction force $P_{FP}$, experiments were conducted as discussed in Section 4. The contact factor $f(d)$ is determined by fitting the model to the experimental data as discussed in Section 6. For this model, only the diameter of the needle and the insertion speed were explored. The needles were inserted into the same tissue under the same conditions. Other factors such as type of tissue, temperature of the tissue, and pre-stress of the tissue were held constant during this study.

## 3. EXPERIMENTAL PROCEDURES

Two experimental procedures were carried out to determine the parameters utilized in the model. In experimental procedure 1 the fracture toughness, frictional force, and crack length were found by inserting a needle into tissue as discussed in Sections 3.1 and shown in Table 1. Experiments used four different needle gauge sizes

(16, 18, 21, and 25) and 4 different speeds (1, 20, 40, and 80 mm/s) with each parameter set run at 5 trials for a total of 80 trials. In experimental procedure 2 the shear modulus was determined by stretching the porcine skin at 4 different strain rates (0.25, 1, 10, and 25 % mm/mm-s) as described in Section 3.2.

### 3.1 Needle Insertion Experiment

The fracture toughness, friction force, and crack length of the tissue were experimentally determined utilizing the needle insertion setup shown in Figure 4. The setup uses a linear motor (Dunkermotoren) to insert the needle into the porcine skin. The porcine skin is mounted between two plates to have consistent boundary conditions across trials. A six-axis force sensor (ATI Industries) records the force on the tissue. Position data was acquired from an encoder located on the linear motor.

For each trial the needle was inserted through the porcine skin, tearing a hole into the skin, and then reinserted through the same hole in the skin. During the initial needle insertion, the total insertion force at puncture, $P$, is due to the fracturing of the tissue, the spreading of the tissue, and friction. In the second insertion the needle is inserted into the exact hole as before producing a force $P'$. Since the crack has already been formed in the first insertion, only the force from spreading the tissue and the friction remain. These forces are equal to the spreading and friction forces of the first insertion. The difference between $P'$ and $P$ is therefore the fracture force. Therefore these forces can be compared as:

$$P'\delta l = \delta \Lambda + P_F\, \delta l \tag{8}$$

Subtracting Equation 8 from Equation 6 yields:

$$(P\text{-}P')\,\delta l = J_{IC}\,a\,\delta l \tag{9}$$

Utilizing Azar and Hayward's method using two insertions, the fracture toughness is able to be extracted when the needle is under steady penetration during a portion of Phase 2, from *x* to *x*' [37]. The region begins after the drop off in force after the initial puncture and ends before the relaxation of the tissue begins. An example plot of the double insertion can be seen in Figure 5(a). The fracture work, the integral of the difference in force *P-P'* with respect to insertion depth, can be seen plotted against the fracture area in Figure 5(b). The crack area was calculated with the crack width results shown later in Section 4.3. The slope of this line yields the fracture toughness $J_{IC}$, as shown in Figure 5(b).

The puncture friction force $P_{FP}$ was acquired during the needle insertion trials. Because the porcine skin has no tissue backing, after the fracture the force drops and levels off. The force occurring in Phase 3, as can be seen in Figure 2, is comprised only of friction force acting on the surface area of the needle along the thickness of the tissue. At this point, no fracture or spreading of tissue is occurring. For this study, the friction measured during Phase 3 was approximated to be the friction occurring at the maximum insertion force during puncture. This approximation was made because the friction during puncture is at its maximum value when it is in contact with the entire thickness of tissue, just as in Phase 3. Although the geometry of the needle in contact with the tissue varies between Phase 2 and Phase 3, the identical tissue thickness will make this an accurate approximation. Separating the friction force during puncture from

the spreading force is a difficult task as they occur simultaneously. The speed dependence of $P_{FP}$ was determined through the needle insertion experiments run at varying speeds.

After needle insertion experiments were performed, the skin was inspected under an optical microscope. The crack length was then measured. An example tissue crack can be seen in Figure 6. Black ink was applied to the needle before insertion to allow for easier visual inspection of the crack length.

### 3.2 Tissue Tension Experiment

The shear modulus was found by performing tension experiments on porcine skin. The experiment utilized the test setup shown in Figure 7. The skin was pulled at strain rates of 0.25, 1, 10, and 25 % mm/mm-s. The results of this experiment were analyzed with an Ogden model to determine the shear modulus and strain hardening properties of the tissue.

Porcine skin is viscoelastic and anisotropic. These properties come from the structure of the skin. The skin consists of stiffer collagen fibers and softer more flexible elastin. The collagen fibers are naturally oriented in a specific direction, along Langer lines, due to the natural pretension of skin. When tensioned, the Young's modulus of the tissue is low to begin because the collagen fibers are moving about each other. Most of the initial stress occurs in the elastin fibers. At higher strains, the fibers become aligned and the tissue stiffens. This creates a J-shape stress-strain curve. As can be seen in Figure 8, the shape of the curve is dependent on the direction the skin is pulled. These

mechanics are strain rate sensitive as well [42]. It has been seen that most biological materials experience shear thinning, thus making it easier to deform them at high strain rates [43].

A sample response of the material with an Ogden fit can be seen in Figure 8. For this study, the shear modulus of the porcine skin is perpendicular to the Langer lines. It is easier for a crack to travel along the collagen fibers than through them, similar to what occurs in bone tissue [44]. Thus, the tissue spreads perpendicular to the Langer lines upon needle insertion. The response can be described by the Ogden model for incompressible, isotropic, hyper-elastic solids. The Ogden fit is used to determine the shear modulus and strain hardening of the skin [45]. The Ogden fit can be written as:

$$\phi = \frac{2\mu}{\alpha^2}\left(\lambda_1^\alpha + \lambda_2^\alpha + \lambda_3^\alpha - 3\right) \tag{10}$$

Where $\phi$ is the strain energy density, $\mu$ is the shear modulus, $\alpha$ is the strain hardening, and $\lambda_i$ are the principle stretch ratios. The one term, one dimension Ogden fit is utilized to determine $\mu$ and $\alpha$:

$$\sigma_z = 2\frac{\mu}{\alpha}\left(\lambda_z^{\alpha-1} + \lambda_z^{-1-\alpha/2}\right) \tag{11}$$

Where $\sigma_z$ and $\lambda_z$ are the stress and stretch ratio in the pull direction respectively. The Ogden equation is fit to the tension test data using least square regression to determine the shear modulus and strain hardening. The one dimensional Ogden fit can closely match the experimental data as shown in the example in Figure 8.

## 4. RESULTS AND DISCUSSION

### 4.1 Fracture Toughness

The results of the fracture toughness trials are shown in Figure 9. As can be seen in the figure, the velocity of the insertion has little effect on the value. The diameter of the needle plays a major role in determining the fracture toughness. A third-degree multivariable (*d* and *v*) polynomial was fit to the data with an $R^2$ value of 0.95. The fit was third ordered across the needle diameters and first ordered across the speeds. The equation for the fitted surface is:

$$J_{IC}(d,v) = 1.305\text{x}10^{7}d + 1.52\text{x}10^{4}v + 3.389\text{x}10^{10}d^{2} - 2.222\text{x}10^{7}dv$$
$$- 1.003\text{x}10^{13}d^{3} + 8.006\text{x}10^{9}d^{2}v \quad (12)$$

The fracture toughness found in this study for hypodermic needles has a complex shape; the 21 gauge needle has the lowest fracture toughness while the 25 gauge needle has the highest. Gokgol et al. found that the measured fracture toughness of round sharp punches decreases linearly with increased diameter [46]. The possibility for difference with our needles is the hypodermic needle is more complex than a round sharp punch. Hypodermic needles have three angles that define their geometry: $\xi_1$, $\xi_2$, and $\beta$, as can be seen in Figure 10 [6]. The three angles were measured for all for needle gauges used in this study and the results are shown in Table 2. It has been seen that different experimental techniques in measuring fracture toughness yield different results [47, 48]. The different angled bevels of the different diameter needles could be affecting the fracture toughness and causing the 21 gauge needle have lower fracture

toughness than the 16 gauge needle. As seen in Table 2, both bevel angles, $\xi_1$ *and* $\xi_2$, are smallest for the 21 gauge needle.

### 4.2 Friction Force

The puncture friction force was recorded and the results are shown in Figure 11. A two-dimensional fit was applied to the data with an $R^2$ value of 0.90. The equation of the fit is:

$$P_{FP}(d, v) = 0.1493 + 365.7d + 0.4463 \ln(v) \quad (13)$$

As in previous studies [8, 21], the experiments show an increase in frictional force with increasing speed. The puncture friction force also increases with increasing needle diameter which is to be expected. A larger needle size has more contact surface area and there is more pressure pushing the needle and tissue together.

### 4.3 Crack Length

The results of the crack length showed a linear trend of increasing crack length for larger needle diameters, as shown in Figure 12 and Equation 14.

$$a(d) = 0.9052\, d \quad (14)$$

Where $a$ is the crack length and $d$ is the diameter of the needle in millimeters. The data is plotted in Figure 12 along with the standard deviation. The smaller crack size than needle diameter occurs because as the needle moves forward, the skin deflects and is stretched before the needle begins to cut. The crack does not run and keep enlarging

because there are many mechanisms found in biological tissues to increase the amount of energy needed to continue fracturing material once a crack is formed, such as the fibers being stretched and therefore helping to round the edge of the crack [43].

### 4.4 Shear Modulus

The shear modulus $\mu$ was measured at four different speeds using the Ogden fit described in Section 4.2. The shear modulus results and standard deviation are plotted in Figure 13. An equation was fit to the data:

$$\mu = -.006\ln(\dot{\varepsilon}) + .087 \tag{15}$$

Where $\mu$ is in MPa and $\dot{\varepsilon}$ is strain rate of insertion in mm/mm-s. The shear modulus decreased as the strain rate increased, confirming that the porcine skin shows shear thinning. The shear modulus was reduced by 36.4% from the 1 mm/s insertion speed to the 80 mm/s speed. The shear modulus values are similar to others in literature [42, 49].

To determine the strain rate $\dot{\varepsilon}$ induced by the needle insertion, it was assumed that the tissue strained perpendicular to the insertion direction. The strain rate of the tissue is proportional to the insertion speed of the needle by the following equation:

$$\dot{\varepsilon} = \frac{v\tan(\beta)}{R_s} \tag{16}$$

Where $\beta$ is the major bevel angle of the needle and $R_s$ is the radius of the hole in the back plate holding the skin, as shown in Figure 4(b). Combining Equation 15 and 16 gives the value of $\mu(v)$ needed for completing the model, Equation 7.

### 4.5 Contact factor

The contact factor $f$ was found by fitting the insertion force model, Equation 7, to the experimental force results. The contact factor was found for each needle gauge size separately using a best fit least-squares regression. The results for the contact factor are shown in Figure 14 and were shown to decrease with increasing diameter based on Equation 17.

$$f = 17.534\, d^{-0.542} \tag{17}$$

## 5. Force Model and Validation

The completed force model, Equation 7, with the values of $J_{IC}(d,v)$ (Equation 12), $a(d)$ (Equation 14), $\mu(v)$ (Equations 15 and 16), $f(d)$ (Equation 17), and $P_{FP}(d,v)$ (Equation 13) is formed and shown in Figure 15 with the experimental results. The model for each needle gauge is within one standard deviation of the experimental data with the largest error being 0.2 N. Equation 7 can be used to determine the portion of the total insertion force represented by each of the three forces acting on the needle as given by Equation 1. The tearing force is given by $J_{IC}(d,v)a(d)$, the spreading force is given by $\mu(v)R^2f(d)$, and the puncture friction force is $P_{FP}$. On average across the four needle sizes, the tearing force accounts for 61% of the total insertion force, the spreading force accounts for 18%, and the friction force accounts for the remaining 21%.

To validate the force model, a 27 gauge hypodermic needle was tested. The needle's outer diameter is 0.41 mm as can be seen in Table 1. The experimental data

was plotted in Figure 16 along with the model's prediction. The over prediction of the model is caused by the complex third degree fit of the fracture toughness overestimating the fracture toughness outside the range of needles tested. However, the model is still within one standard deviation for each data point with all the errors less than the 0.2 N maximum error of the trials used to create the model.

## 6. CONCLUSIONS

A dynamic physics-based model was constructed and shown to accurately predict insertion forces upon needle insertion into porcine skin for four different gauge hypodermic needles. The model shows that on average, 61% of the total insertion force comes from creating the crack. Friction contributes 21% of the total force and the spreading of the tissue contributes 18% of the force. For porcine skin, increasing the insertion speed did not lower the insertion force. From the experimental results, it is evident that fracture toughness is relatively constant across different insertion speeds. It was also shown that increasing insertion speed increases the frictional force on the needle. Increasing speeds were shown to benefit in reducing the spreading force of the tissue to accommodate the needle.

**ACKNOWLEDGMENT**

This material is based upon work supported by the National Science Foundation under Grant No. CMMI-1404916.

## References

[1] Abolhassani, N., Patel, R., and Moallem, M., 2007, "Needle Insertion into Soft Tissue: A Survey," Medical engineering & physics, 29(4), pp. 413-431.

[2] Egekvist, H., Bjerring, P., and Arendt-Nielsen, L., 1999, "Pain and Mechanical Injury of Human Skin Following Needle Insertions," European Journal of Pain, 3(1), pp. 41-49.

[3] Dimaio, S. P., and Salcudean, S. E., 2003, "Needle Insertion Modeling and Simulation," IEEE Transactions on Robotics and Automation, 19(5), pp. 864-875.

[4] Ehmann, K., and Malukhin, K., 2012, "A Generalized Analytical Model of the Cutting Angles of a Biopsy Needle Tip," Journal of Manufacturing Science and Engineering-Transactions of the Asme, 134(6).

[5] Moore, J. Z., Zhang, Q. H., Mcgill, C. S., Zheng, H. J., Mclaughlin, P. W., and Shih, A. J., 2010, "Modeling of the Plane Needle Cutting Edge Rake and Inclination Angles for Biopsy," Journal of Manufacturing Science and Engineering-Transactions of the Asme, 132(5).

[6] Wang, Y. C., Tai, B. L., Chen, R. K., and Shih, A. J., 2013, "The Needle with Lancet Point: Geometry for Needle Tip Grinding and Tissue Insertion Force," Journal of Manufacturing Science and Engineering-Transactions of the Asme, 135(4).

[7] Moore, J. Z., Mclaughlin, P. W., and Shih, A. J., 2012, "Novel Needle Cutting Edge Geometry for End-Cut Biopsy," Medical Physics, 39(1), pp. 99-108.

[8] Okamura, A. M., Simone, C., and O'leary, M. D., 2004, "Force Modeling for Needle Insertion into Soft Tissue," IEEE Transactions on Biomedical Engineering, 51(10), pp. 1707-1716.

[9] Vedrine, L., Prais, W., Laurent, P. E., Raynal-Olive, C., and Fantino, M., 2003, "Improving Needle-Point Sharpness in Prefillable Syringes," Med Device Technol, 14(4), pp. 32-5.

[10] Davis, S. P., Landis, B. J., Adams, Z. H., Allen, M. G., and Prausnitz, M. R., 2004, "Insertion of Microneedles into Skin: Measurement and Prediction of Insertion Force and Needle Fracture Force," Journal of Biomechanics, 37(8), pp. 1155-1163.

[11] Kim, Y. C., Park, J. H., and Prausnitz, M. R., 2012, "Microneedles for Drug and Vaccine Delivery," Advanced Drug Delivery Reviews, 64(14), pp. 1547-1568.

[12] Han, P. D., and Ehmann, K., 2013, "Study of the Effect of Cannula Rotation on Tissue Cutting for Needle Biopsy," Medical Engineering & Physics, 35(11), pp. 1584-1590.

[13] Wedlick, T. R., and Okamura, A. M., 2012, "Characterization of Robotic Needle Insertion and Rotation in Artificial and Ex Vivo Tissues," 2012 4th IEEE Ras & Embs International Conference on Biomedical Robotics and Biomechatronics (Biorob), pp. 62-68.

[14] Barnett, A. C., Wolkowicz, K., and Moore, J. Z., 2014, "Vibrating Needle Cutting Force," eds., pp. V002T02A025-V002T02A025.

[15] Begg, N. D. M., and Slocum, A. H., 2014, "Audible Frequency Vibration of Puncture-Access Medical Devices," Medical Engineering & Physics, 36(3), pp. 371-377.

[16] Huang, Y. C., Tsai, M. C., and Lin, C. H., 2012, "A Piezoelectric Vibration-Based Syringe for Reducing Insertion Force," International Symposium on Ultrasound in the Control of Industrial Processes (Ucip 2012), 42.

[17] Izumi, H., Yajima, T., Aoyagi, S., Tagawa, N., Arai, Y., and Hirata, M., 2008, "Combined Harpoonlike Jagged Microneedles Imitating Mosquito's Proboscis and Its Insertion Experiment with Vibration," IEEJ Transactions on Electrical and Electronic Engineering, 3(4), pp. 425-431.

[18] Yang, M., and Zahn, J. D., 2004, "Microneedle Insertion Force Reduction Using Vibratory Actuation," Biomedical Microdevices, 6(3), pp. 177-182.

[19] Heverly, M., Dupont, P., and Triedman, J., 2005, "Trajectory Optimization for Dynamic Needle Insertion," 2005 IEEE International Conference on Robotics and Automation (Icra), Vols 1-4, pp. 1646-1651.

[20] Mahvash, M., and Dupont, P. E., 2009, "Fast Needle Insertion to Minimize Tissue Deformation and Damage," Icra: 2009 IEEE International Conference on Robotics and Automation, Vols 1-7, pp. 2761-2766.

[21] Kobayashi, Y., Sato, T., and Fujie, M. G., 2009, "Modeling of Friction Force Based on Relative Velocity between Liver Tissue and Needle for Needle Insertion Simulation," 2009 Annual International Conference of the IEEE Engineering in Medicine and Biology Society, Vols 1-20, pp. 5274-5278.

[22] Abolhassani, N., Patel, R., and Moallem, M., 2004, "Trajectory Generation for Robotic Needle Insertion in Soft Tissue," Proceedings of the 26th Annual International Conference of the IEEE Engineering in Medicine and Biology Society, Vols 1-7, 26, pp. 2730-2733.

[23] Frick, T. B., Marucci, D. D., Cartmill, J. A., Martin, C. J., and Walsh, W. R., 2001, "Resistance Forces Acting on Suture Needles," Journal of Biomechanics, 34(10), pp. 1335-1340.

[24] Koelmans, W., Krishnamoorthy, G., Heskamp, A., Wissink, J., Misra, S., and Tas, N., 2013, "Microneedle Characterization Using a Double-Layer Skin Simulant," Mechanical Engineering Research, 3(2), pp. p51.

[25] Crouch, J. R., Schneider, C. M., Wainer, J., and Okamura, A. M., 2005, "A Velocity-Dependent Model for Needle Insertion in Soft Tissue," Medical Image Computing and Computer-Assisted Intervention - Miccai 2005, Pt 2, 3750, pp. 624-632.

[26] Yan, K. G., Podder, T., Yu, Y., Liu, T.-I., Cheng, C. W. S., and Ng, W. S., 2009, "Flexible Needle–Tissue Interaction Modeling with Depth-Varying Mean Parameter: Preliminary Study," Biomedical Engineering, IEEE Transactions on, 56(2), pp. 255-262.

[27] Dehghan, E., Wen, X., Zahiri-Azar, R., Marchal, M., and Salcudean, S. E., 2007, "Modeling of Needle-Tissue Interaction Using Ultrasound-Based Motion Estimation," Medical Image Computing and Computer-Assisted Intervention - MICCAI 2007, Pt 1, Proceedings, 4791, pp. 709-716.

[28] Roesthuis, R. J., Van Veen, Y. R., Jahya, A., and Misra, S., 2011, "Mechanics of Needle-Tissue Interaction," eds., pp. 2557-2563.

[29] Shergold, O. A., and Fleck, N. A., 2004, "Mechanisms of Deep Penetration of Soft Solids, with Application to the Injection and Wounding of Skin," Proceedings of the Royal Society a-Mathematical Physical and Engineering Sciences, 460(2050), pp. 3037-3058.

[30] Misra, S., Reed, K. B., Schafer, B. W., Ramesh, K. T., and Okamura, A. M., 2010, "Mechanics of Flexible Needles Robotically Steered through Soft Tissue," International Journal of Robotics Research, 29(13), pp. 1640-1660.

[31] Mahvash, M., and Dupont, P. E., 2010, "Mechanics of Dynamic Needle Insertion into a Biological Material," IEEE Transactions on Biomedical Engineering, 57(4), pp. 934-943.

[32] Anderson, T. L., 2005, *Fracture Mechanics: Fundamentals and Applications*, CRC press.

[33] Atkins, A. G., and Mai, Y.-W., 1985, *Elastic and Plastic Fracture: Metals, Polymers, Ceramics, Composites, Biological Materials*, Ellis Horwood; Halsted Press.

[34] Atkins, A. G., 2005, "Toughness and Cutting: A New Way of Simultaneously Determining Ductile Fracture Toughness and Strength," Engineering Fracture Mechanics, 72(6), pp. 849-860.

[35] Liu, J., Bai, Y. L., and Xu, C. Y., 2014, "Evaluation of Ductile Fracture Models in Finite Element Simulation of Metal Cutting Processes," Journal of Manufacturing Science and Engineering-Transactions of the Asme, 136(1).

[36] Orlowski, K. A., Ochrymiuk, T., Atkins, A., and Chuchala, D., 2013, "Application of Fracture Mechanics for Energetic Effects Predictions While Wood Sawing," Wood Science and Technology, 47(5), pp. 949-963.

[37] Azar, T., and Hayward, V., 2008, "Estimation of the Fracture Toughness of Soft Tissue from Needle Insertion," Biomedical Simulation, Proceedings, 5104, pp. 166-175.

[38] Mahvash, M., and Hayward, V., 2001, "Haptic Rendering of Cutting: A Fracture Mechanics Approach," Haptics-e, 2(3), pp. 1-12.

[39] Shergold, O. A., and Fleck, N. A., 2005, "Experimental Investigation into the Deep Penetration of Soft Solids by Sharp and Blunt Punches, with Application to the Piercing of Skin," Journal of Biomechanical Engineering-Transactions of the Asme, 127(5), pp. 838-848.

[40] Asadian, A., Patel, R. V., and Kermani, M. R., 2011, "A Distributed Model for Needle-Tissue Friction in Percutaneous Interventions," 2011 IEEE International Conference on Robotics and Automation (Icra), pp. 1896-1901.

[41] Ankersen, J., Birkbeck, A. E., Thomson, R. D., and Vanezis, P., 1999, "Puncture Resistance and Tensile Strength of Skin Simulants," Proceedings of the Institution of Mechanical Engineers Part H-Journal of Engineering in Medicine, 213(H6), pp. 493-501.

[42] Zhou, B., Xu, F., Chen, C. Q., and Lu, T. J., 2010, "Strain Rate Sensitivity of Skin Tissue under Thermomechanical Loading," Philosophical Transactions of the Royal Society a-Mathematical Physical and Engineering Sciences, 368(1912), pp. 679-690.

[43] Vincent, J., 2012, *Structural Biomaterials*, Princeton University Press.

[44] Nalla, R. K., Stolken, J. S., Kinney, J. H., and Ritchie, R. O., 2005, "Fracture in Human Cortical Bone: Local Fracture Criteria and Toughening Mechanisms," Journal of Biomechanics, 38(7), pp. 1517-1525.

[45] Ogden, R. W., Saccomandi, G., and Sgura, I., 2004, "Fitting Hyperelastic Models to Experimental Data," Computational Mechanics, 34(6), pp. 484-502.

[46] Gokgol, C., Basdogan, C., and Canadinc, D., 2012, "Estimation of Fracture Toughness of Liver Tissue: Experiments and Validation," Medical engineering & physics, 34(7), pp. 882-891.

[47] Pereira, B. P., Lucas, P. W., and Sweehin, T., 1997, "Ranking the Fracture Toughness of Thin Mammalian Soft Tissues Using the Scissors Cutting Test," Journal of Biomechanics, 30(1), pp. 91-94.

[48] Purslow, P. P., 1983, "Measurement of the Fracture-Toughness of Extensible Connective Tissues," Journal of Materials Science, 18(12), pp. 3591-3598.

[49] Shergold, O. A., Fleck, N. A., and Radford, D., 2006, "The Uniaxial Stress Versus Strain Response of Pig Skin and Silicone Rubber at Low and High Strain Rates," International Journal of Impact Engineering, 32(9), pp. 1384-1402.

**NOMENCLATURE**

| | |
|---|---|
| $a$ | Length of crack in the tissue |
| $\alpha$ | Strain hardening factor |
| $\beta$ | Rotation angle of lancets |
| $d$ | Outer diameter of the needle |
| $\dot{\varepsilon}$ | Strain rate of the tissue |
| $f$ | Contact factor |
| $J_{IC}$ | Mode I fracture toughness of the tissue |
| $I$ | Insertion depth of the needle |
| $\Lambda$ | Strain energy stored in tissue |
| $\lambda_i$ | Principle stretch ratios |
| $\lambda_z$ | Stretch ratio in the z (pull) direction |
| $\mu$ | Shear modulus of the tissue |
| $N$ | Number of termed Ogden fit |
| $P$ | Total insertion force |
| $P'$ | Insertion force of second insertion |
| $P_t$ | Tearing Force |
| $P_F$ | Friction Force |
| $P_{FP}$ | Puncture Friction Force |
| $P_s$ | Spreading Force |
| $\phi$ | Strain energy density |
| $\varphi$ | Secondary bevel angle |
| $R$ | Outer radius of the needle |
| $R_s$ | Radius of back skin plate hole |

| | |
|---|---|
| $\sigma_z$ | Stress in the z (pull) direction |
| $v$ | Needle insertion velocity |
| $W_R$ | Energy released by crack formation |
| $x$ | Position of start of steady needle penetration |
| $x'$ | Position of end of steady needle penetration |
| $\xi_1$ | Primary bevel angle of the needle |
| $\xi_2$ | Secondary bevel angle of the needle |
| $y$ | Axis initially normal to major bevel angle |
| $y'$ | Axis normal to major bevel after rotation |

# Figure Caption List

**FIGURE 1.** Needle position inaccuracy due to (a) the needle bending and (b) target position movement

**FIGURE 2.** Force profile of needle passing through porcine skin

**FIGURE 3.** Forces that compose total cutting force

**FIGURE 4.** (a) Experimental setup for needle insertion and (b) porcine skin mounting

**FIGURE 5.** (a) Graph of 1st and 2nd needle insertion and (b) graph of fracture work performed to determine $J_{IC}$

**FIGURE 6.** Measured needle crack length in porcine skin

**FIGURE 7.** Experimental setup for stretching porcine skin to determine shear modulus

**FIGURE 8.** Stress-strain curve of the porcine skin parallel, at a 45° angle, and perpendicular (including Ogden Fit) to the Langer lines

**FIGURE 9.** Fracture toughness of varying gauge needles from 1 to 80 mm/s

**FIGURE 10.** Definition of the three angles that define hypodermic needle geometry

**FIGURE 11.** Two-dimensional fit of friction data where the points are the experimental data and the surface is the best fit

**FIGURE 12.** Tissue crack length results with linear fit

**FIGURE 13.** Measured shear modulus compared to strain rate

**FIGURE 14.** Contact factor *f* compared to needle outer diameter

**FIGURE 15.** Completed force model (lines) plotted against experimental needle insertion force results (points)

**FIGURE 16.** Completed force model (line) plotted against experimental needle insertion force result (point) for 27 gauge needle

## Table Caption List

**Table 1.** Experimental procedure 1, needle insertion into porcine skin

**Table 2.** Measured angles of hypodermic needles

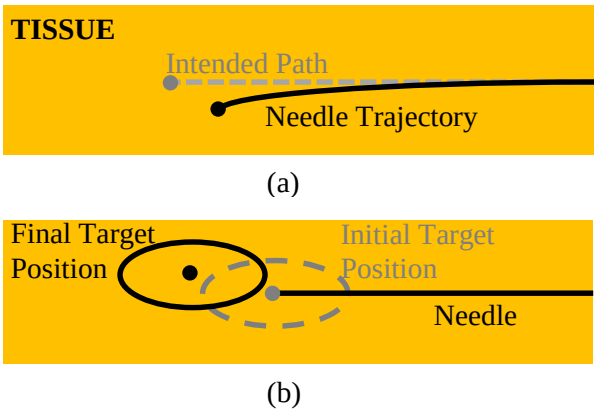


**FIGURE 1.** Needle position inaccuracy due to (a) the needle bending and (b) target position movement

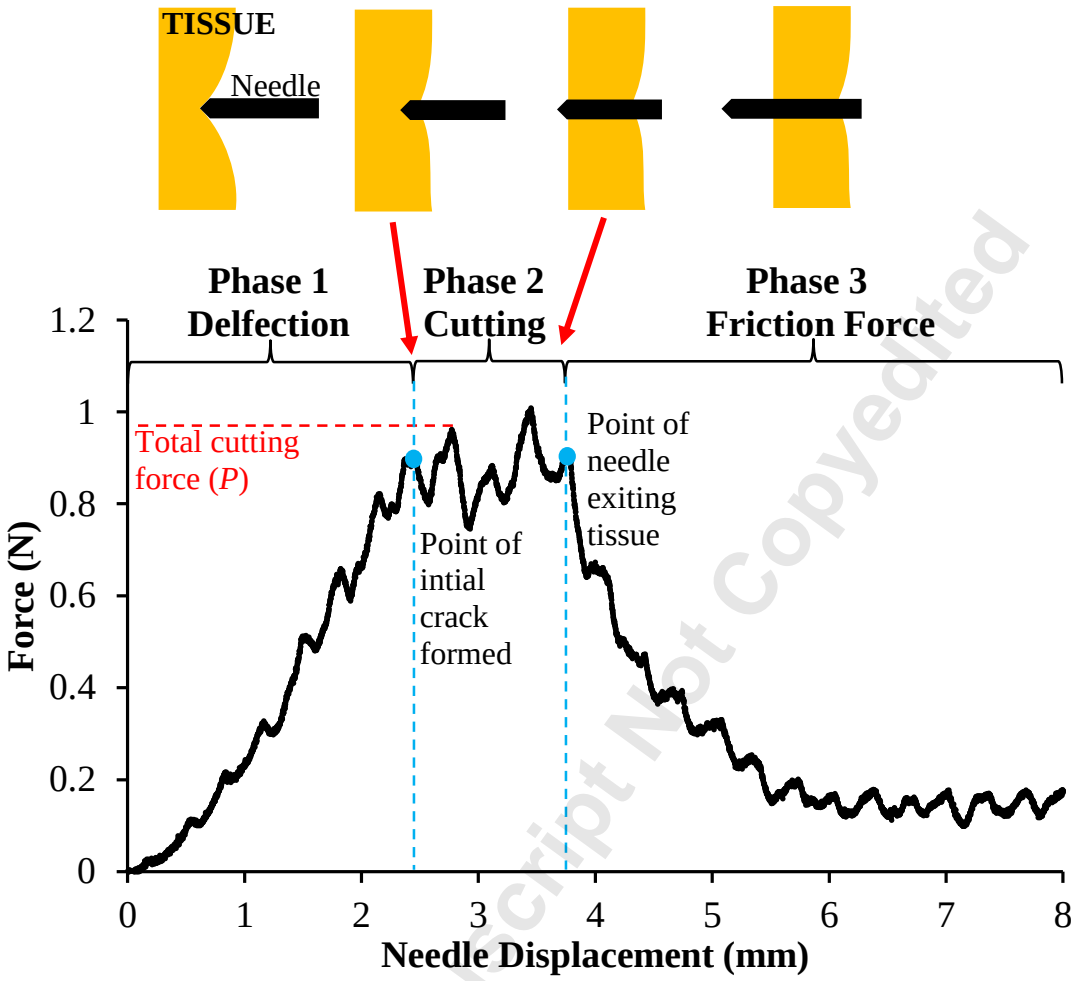


**FIGURE 2.** Force profile of needle passing through porcine skin

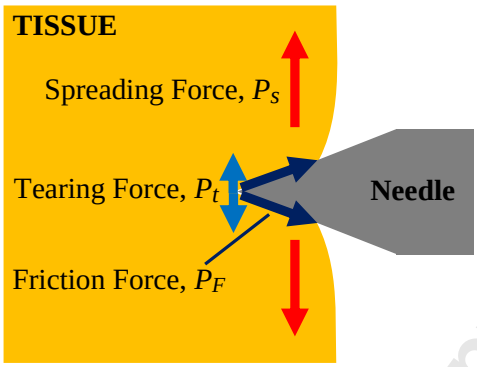


**FIGURE 3.** Forces that compose total cutting force

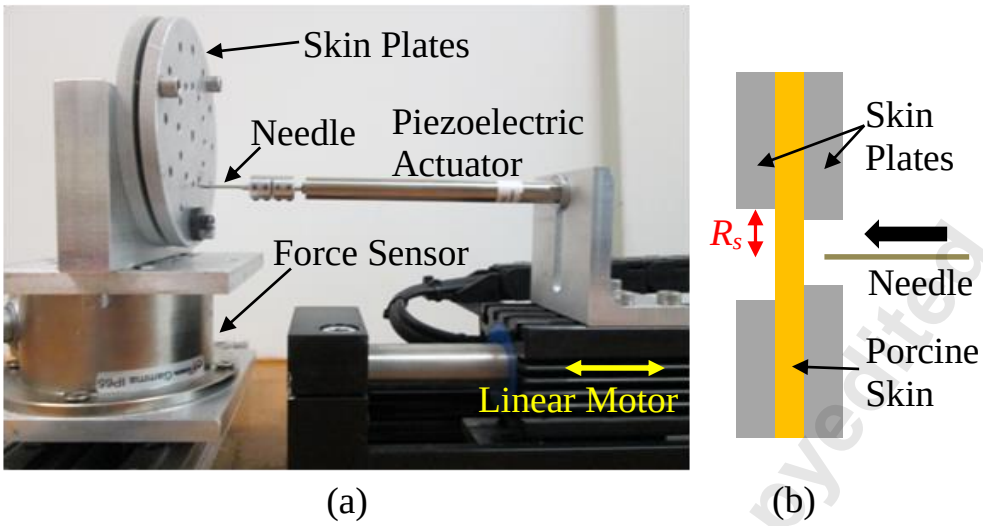


**FIGURE 4.** (a) Experimental setup for needle insertion and (b) porcine skin mounting

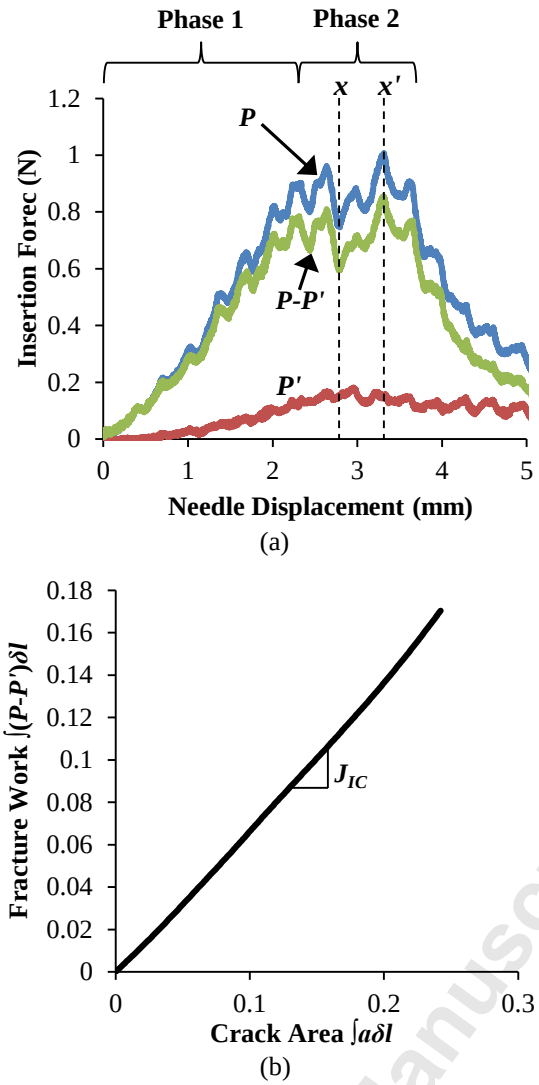


**FIGURE 5.** (a) Graph of 1st and 2nd needle insertion and (b) graph of fracture work performed to determine $J_{IC}$

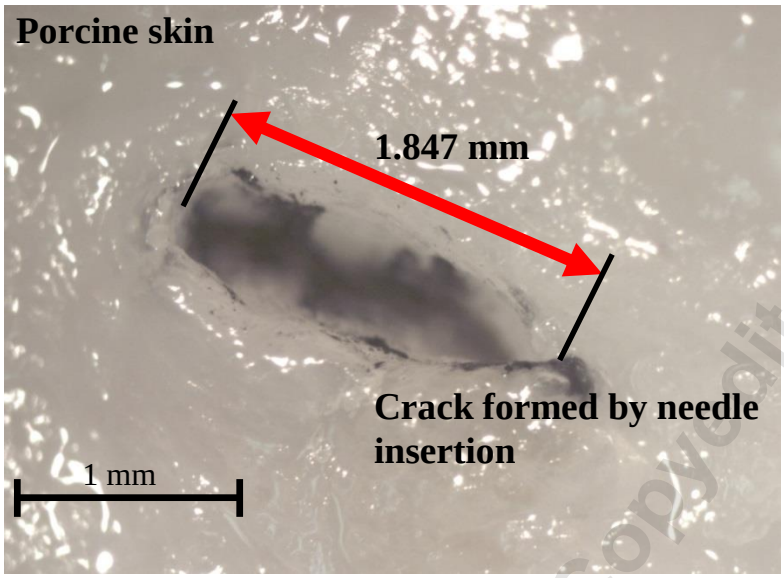


**FIGURE 6**. Measured needle crack length in porcine skin

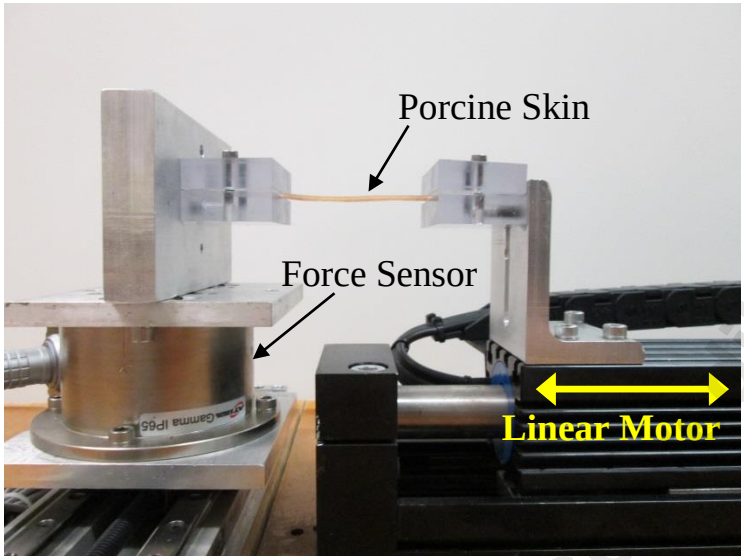


**FIGURE 7.** Experimental setup for stretching porcine skin to determine shear modulus

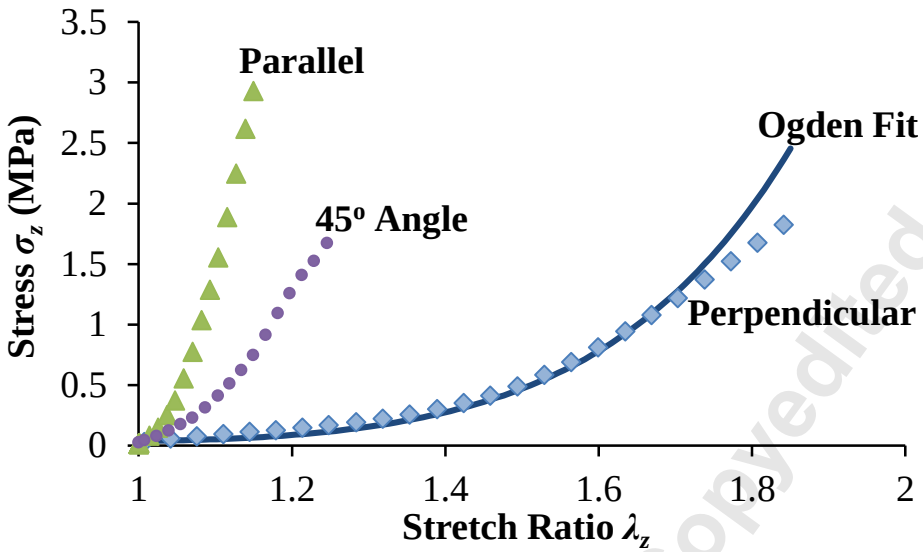


**FIGURE 8.** Stress-strain curve of the porcine skin parallel, at a 45° angle, and perpendicular (including Ogden Fit) to the Langer lines

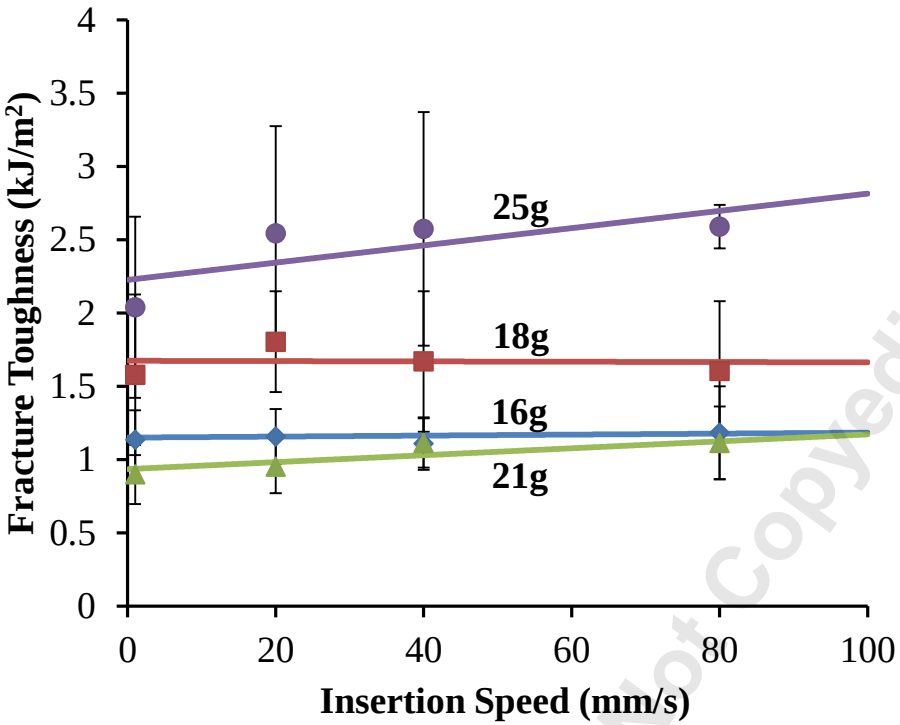


**FIGURE 9.** Fracture toughness of varying gauge needles from 1 to 80 mm/s

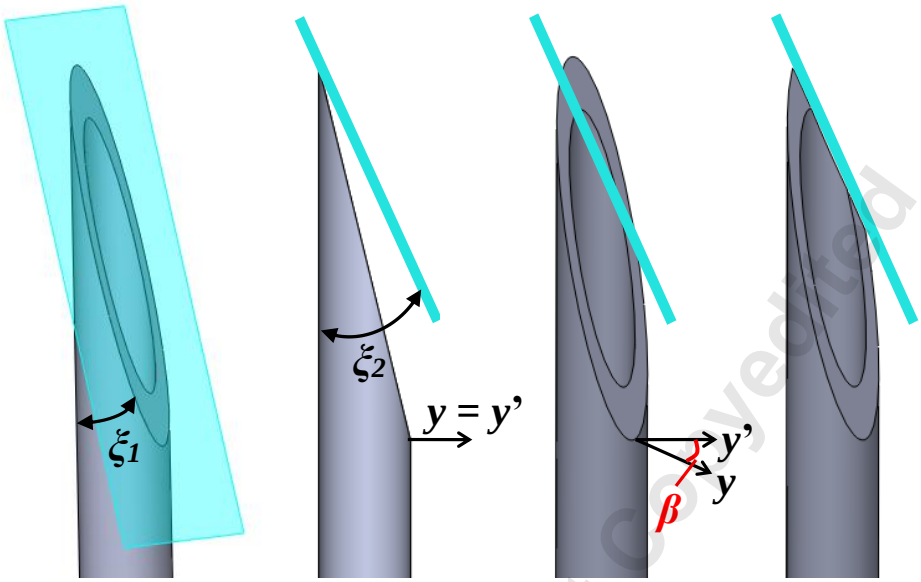


**FIGURE 10.** Definition of the three angles that define hypodermic needle geometry

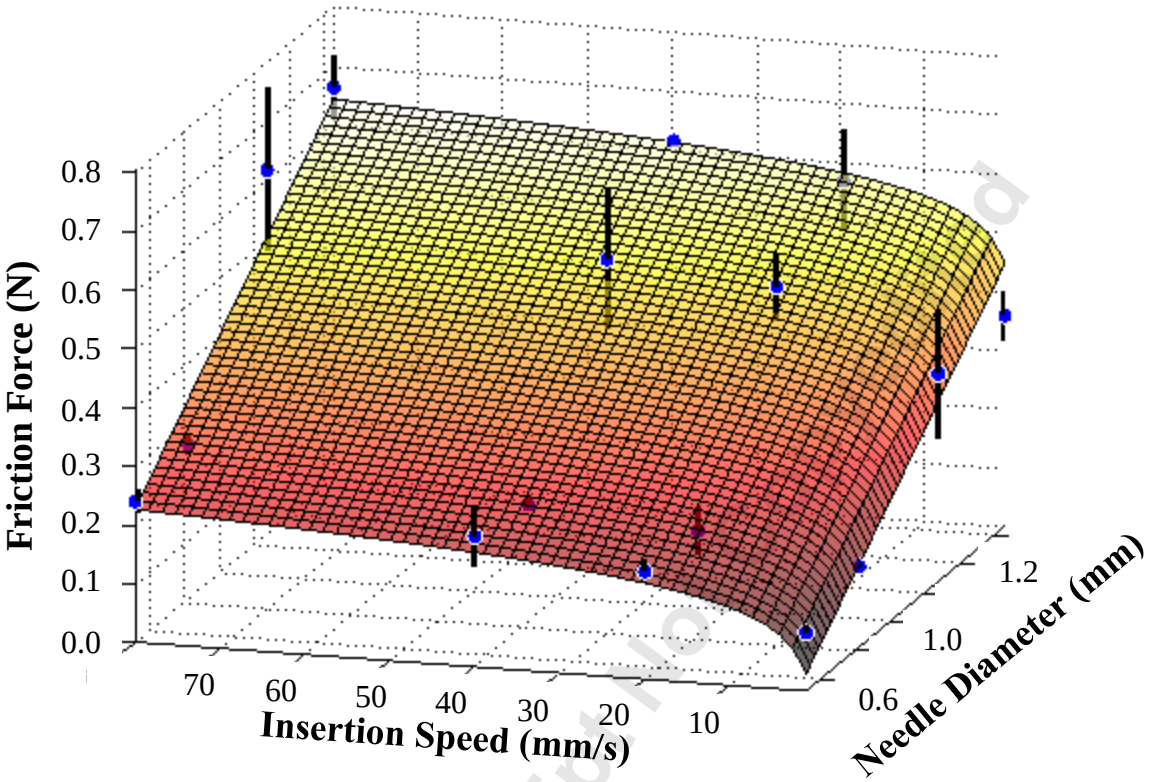


**FIGURE 11.** Two-dimensional fit of friction data where the points are the experimental data and the surface is the best fit

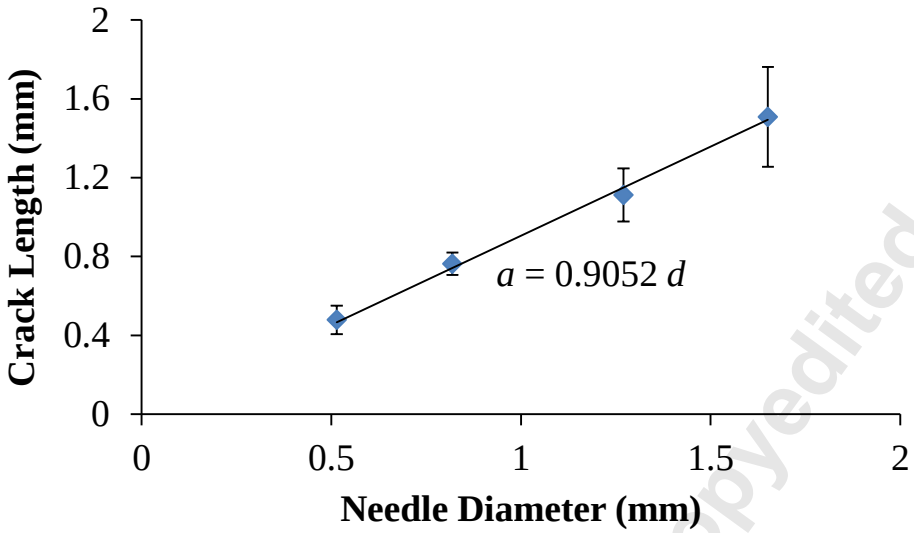


**FIGURE 12.** Tissue crack length results with linear fit

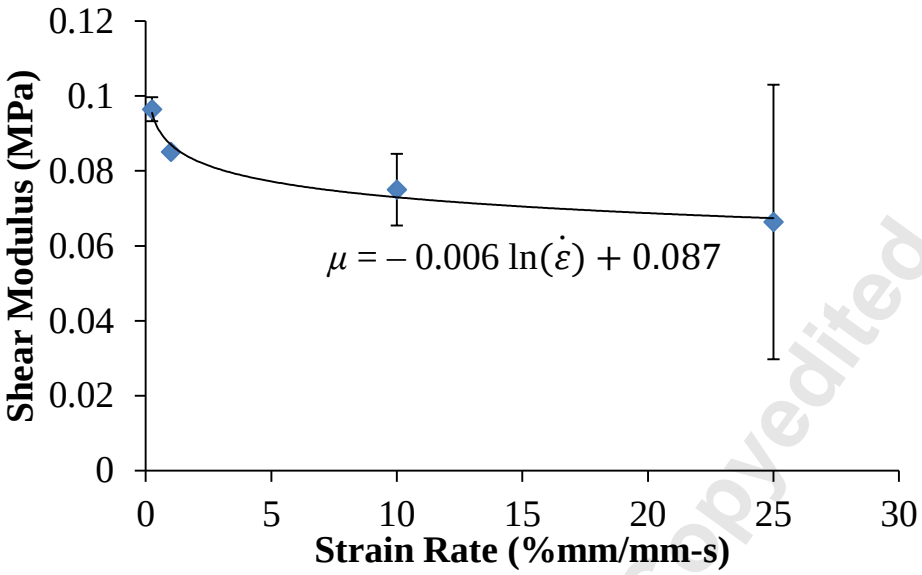


**FIGURE 13.** Measured shear modulus compared to strain rate

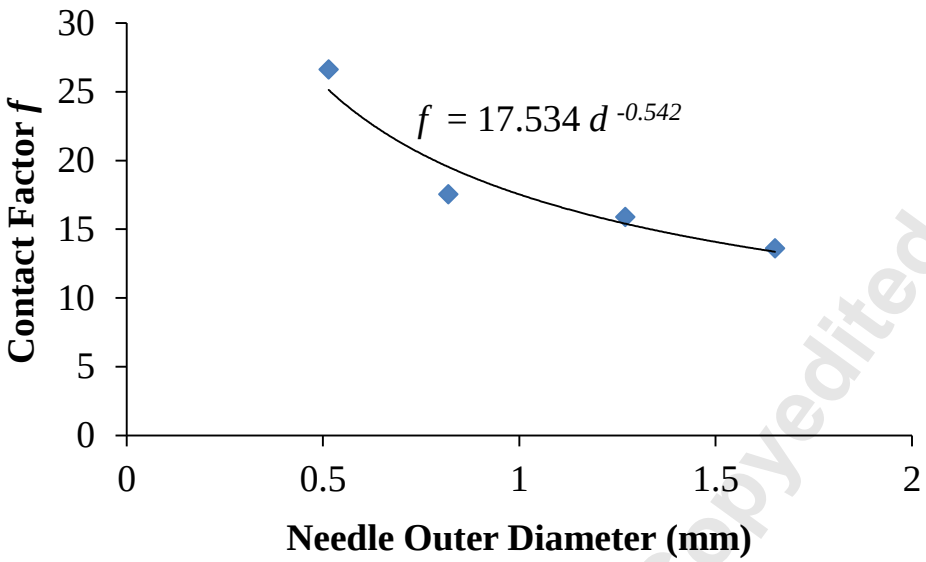


**Figure 14.** Contact factor *f* compared to needle outer diameter

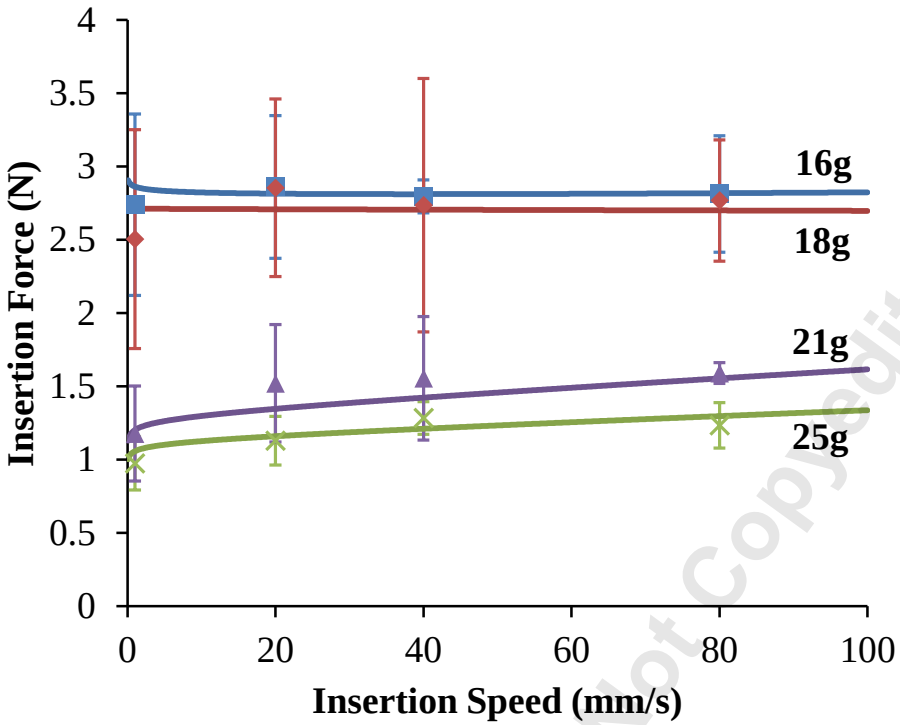


**FIGURE 15.**

Completed force model (lines) plotted against experimental needle insertion force results (points)

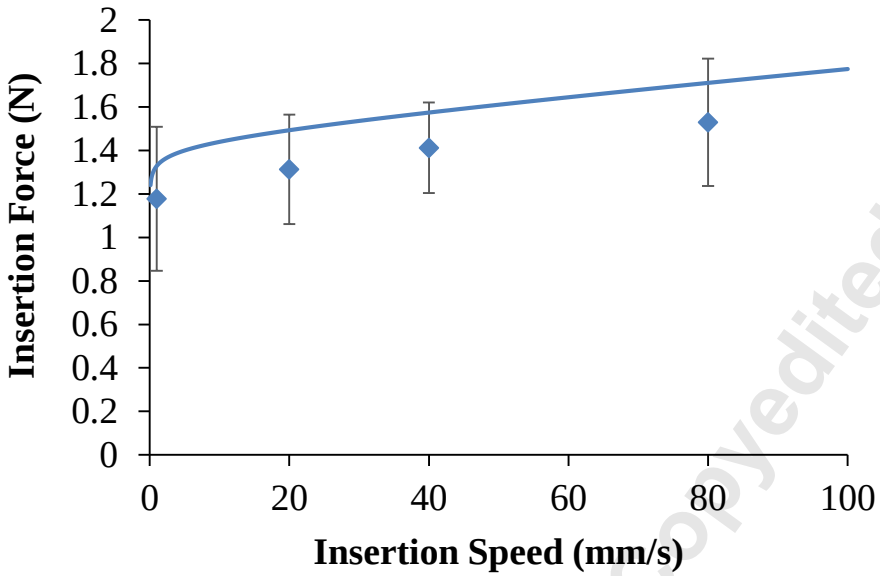


**FIGURE 16.** Completed force model (line) plotted against experimental needle insertion force result (point) for 27 gauge needle

**Table 1.** Experimental procedure 1, needle insertion into porcine skin

| Needle Gauge | Needle Outer Diameter (mm) | Insertion Speed (mm/s) | Number of Trials |
|---|---|---|---|
| 16 | 1.65 | 1, 20, 40, and 80 | 5 |
| 18 | 1.27 | | |
| 21 | 0.82 | | |
| 25 | 0.51 | | |
| 27 | 0.41 | | |

**Table 2.** Measured angles of hypodermic needles

| Needle Gauge | $\xi_1$ | $\xi_2$ | $\beta$ |
|---|---|---|---|
| 16 | 9.9° | 17.5° | 53.0° |
| 18 | 10.6° | 21.5° | 48.5° |
| 21 | 9.4° | 16.0° | 46.5° |
| 25 | 9.6° | 18.5° | 43.0° |